The near-surface electron radiation environment of Saturn's moon Mimas

T.A. Nordheim[1*], K.P. Hand[1], C. Paranicas[2], C. J. A. Howett[3], A. R. Hendrix[4], G.H. Jones[5,6], A. J. Coates[5,6]

[1]Jet Propulsion Laboratory, California Institute of Technology, 4800 Oak Grove Drive, Pasadena, CA 91109, USA.

[2]Applied Physics Laboratory, John Hopkins University, 11100 John Hopkins Road, Laurel, MD 20723, USA

[3]Southwest Research Institute, 1050 Walnut Street, Suite 300, Boulder, CO 80304, USA.

[4]Planetary Science Institute, 1700 East Fort Lowell, Suite 106, Tucson, AZ 85719, USA.

[5]Mullard Space Science Laboratory, University College London, Dorking, Surrey RH5 6NT, UK

[6]Centre for Planetary Sciences at UCL/Birkbeck, University College London, Gower Street, London WC1E 6BT, UK

* Corresponding author: Phone +1 818 393 8037

email: tom.nordheim@jpl.nasa.gov

Abstract

Saturn's inner mid-size moons are exposed to a number of external weathering processes, including charged particle bombardment and UV photolysis, as well as deposition of E-ring grains and interplanetary dust. While optical remote sensing observations by several instruments onboard the *Cassini* spacecraft have revealed a number of weathering patterns across the surfaces of these moons, it is not entirely clear which external process is responsible for which observed weathering pattern. Here we focus on Saturn's moon Mimas and model the effect of energetic electron bombardment across its surface. By using a combination of a guiding center, bounce-averaged charged particle tracing approach and a particle physics code, we investigate how the radiation dose due to energetic electrons is deposited with depth at different locations. We predict a lens-shaped electron energy deposition pattern that extends down to ~cm depths at low latitudes centered around the apex of the leading hemisphere (90° W). These results are consistent with previous remote sensing observations of a lens-shaped color anomaly observed by the Imaging Science Subsystem (ISS) instrument as well as a thermal inertia anomaly observed by the Visual and Infrared Mapping Spectrometer (VIMS) and the Composite Infrared Spectrometer (CIRS). Our results confirm that these features are produced by MeV electrons that have a penetration depth into the surface comparable to the effective sampling depths of these instruments. On the trailing hemisphere we predict a similar lens-shaped electron energy deposition pattern, whose effects have to date not been observed by the *Cassini* remote sensing

instruments. We suggest that no corresponding lens-shaped weathering pattern has been observed on the trailing hemisphere because of the comparatively short range of lower energy (<1 MeV) electrons into surface ice, as well as competing effects from cold plasma, neutral, and dust bombardment.

Introduction

Mimas is Saturn's innermost mid-sized moon and orbits at a distance of 3.08 Saturn radii (R_S), near the inner edge of the E-ring. Its surface is heavily cratered, without any obvious signs of recent geological activity, and it has a surface composition that is dominated by H_2O ice (e.g. Filacchione et al., 2007). However, the surface is exposed to a number of external weathering agents, including deposition of E-ring grains, photolysis, micrometeoroid impact gardening and bombardment by magnetospheric particles. As these processes operate at different spatial and temporal scales, detailed modeling of each is required to fully understand the present-day state of the surface, and to effectively interpret the observations made by the remote sensing instruments on *Cassini*.

In observations of Tethys by the *Voyager* spacecraft, a lens-shaped equatorial band was found on the leading hemisphere of that moon (Buratti et al., 1990; Smith et al., 1981). Schenk et al. (2011) later surveyed several of Saturn's icy satellites using data from the *Cassini* Imaging Science Subsystem (ISS) and found a lens-shaped color anomaly on the leading hemispheres of Mimas, and confirmed the Tethys lens-shaped feature, in ratio maps using the instrument's IR3 (930 nm) and UV3 (338 nm) filters. In these observations, the color anomaly appeared as a bright feature at 338 nm, implying that enhanced scattering is occurring at these wavelengths and that the feature is therefore "blueish" in color. A thermal inertia anomaly was later found at low latitudes on the leading hemispheres of Mimas, Tethys and Dione using the Composite Infrared Spectrometer (CIRS) (Howett et al., 2012a, 2012b, 2011). At Mimas and Tethys, the anomalous region is roughly co-located with the leading hemisphere color anomaly observed by ISS (Howett et al., 2012a, 2011). The day and night time temperatures inside these anomalous regions are consistent with a thermal conductivity that is ~ 25x higher than surrounding regions. At Dione, a weak thermal inertia anomaly is observed by CIRS, but no color anomaly is detected by ISS

(Howett et al., 2012b). A thermal inertia anomaly is also present at Rhea's leading hemisphere, however, unlike the lens-shaped anomalies at Mimas, Tethys and Dione, it is here associated with a geologic feature (a crater ejecta blanket) (Howett et al., 2012b). Using the spectral position of the 3.6 μm continuum peak in water ice, Filacchione et al. (2016) derived daytime surface temperature maps of Saturn's icy satellites using the Visual and Infrared and Mapping Spectrometer (VIMS) (Brown et al., 2005). Like CIRS, VIMS observed thermally anomalous regions at the leading hemisphere equator of Mimas and Tethys, however, unlike CIRS, VIMS does not observe a thermal anomaly at Dione's leading hemisphere. Observations of Mimas by the Cassini Ultraviolet Imaging Spectrograph (UVIS) did not reveal a clear signature of the leading hemisphere lens, although a faint signature of what may be one of the ansae (low latitude edges) of the lens was reported (Hendrix et al., 2012).

The lens features on Mimas, Tethys and Dione have been attributed to the action of ~MeV electrons, which preferentially bombard the leading hemisphere of these satellites and have a penetration range into the surface comparable to the effective sampling depths of the ISS and CIRS observations (Howett et al., 2011; Paranicas et al., 2014; Schenk et al., 2011). In the context of the CIRS and VIMS observations of surface temperatures, it has been suggested that the energetic electrons may sinter ice grains together, thus increasing the grain contact boundaries and the thermal conductivity (Howett et al., 2011; Schaible et al., 2016). With regards to the ISS color anomaly, it has been proposed that the electrons produce defects and small voids in surface ice, leading to enhanced scattering at the wavelengths relevant to the ISS UV3 filter (Schenk et al., 2011). However, no comprehensive quantitative modeling has thus far been carried out to investigate the modification of surface- and near-surface ice on the saturnian satellites by energetic electrons.

The observed lens feature anomalies appear to match contours of energetic electron flux at the surface of these moons (Paranicas et al., 2014; Schenk et al., 2011). At Mimas and Tethys, the observed ISS color anomaly appears to roughly correspond to regions of the surface that receive an electron energy flux of > $10^{4.5}$ MeV cm^{-2} s^{-1}. However, while the corresponding leading hemisphere region on Dione receives a similar electron energy flux as Tethys, no ISS lens feature is observed, and only a weak thermal anomaly is seen by CIRS. This is an ongoing puzzle in the interpretation of the remote sensing observations using the electron lens idea. As discussed by Paranicas et al. (2014), this may be due to the fact that the leading hemisphere of Dione receives a larger fraction of the dose from slightly lower energy electrons, which have a shorter penetration ranges into the surface. In addition, the saturnian magnetic field is more variable near Dione than it is near Mimas, and it is possible that the electron drift paths are not as consistent over time. Furthermore, the magnitude of the leading hemisphere thermal inertia anomaly is observed to decrease as we move outwards from Mimas, with the anomaly only slightly above background values at Dione and no similar lens-shaped anomaly detected at Rhea (Howett et al., 2012b). These effects are not explained by the surface electron flux contours and illustrate why knowledge of the *dose versus depth* is crucially important, as particles of different energies and species will deliver their main dose at different depths into the surface. Such spatially resolved dose versus depth profiles are therefore essential for any quantitative discussion of surface modification by energetic electrons, as well as to establish a correlation between radiation effects and remote sensing observations. In the present work we investigate energetic electron weathering at Saturn's icy moons by modelling the three-dimensional bombardment of energetic electrons across the surface, including the interaction of these particles with the uppermost subsurface. Here we have focused on characterizing the near-surface electron radiation environment at the moon Mimas and discuss our modelling results in the context of the previously reported remote sensing observations.

1. Modeling approach

Charged particles in the saturnian magnetosphere have three fundamental motions: gyration about magnetic field lines, bounce between magnetic mirror points and longitudinal motion. The longitudinal motion is the sum of the drifts due to the co-rotation electric field and the gradient and curvature of magnetic field lines (gradient-curvature drift). The co-rotation drift at Saturn is eastwardly directed and causes ions and electrons to overtake the moons in their orbits, thus preferentially bombarding their trailing hemispheres. For electrons, the gradient-curvature drift is opposite to corotation, and above some critical energy, termed the keplerian resonance energy, this drift causes electrons to have net retrograde motion relative to the moons (Roussos et al., 2007; Thomsen and Van Allen, 1980). Thus, as illustrated in Figure 1, while the moons' trailing hemispheres are bombarded by co-rotating plasma and lower-energy energetic electrons, the leading hemispheres are primarily exposed to high energy energetic electrons.

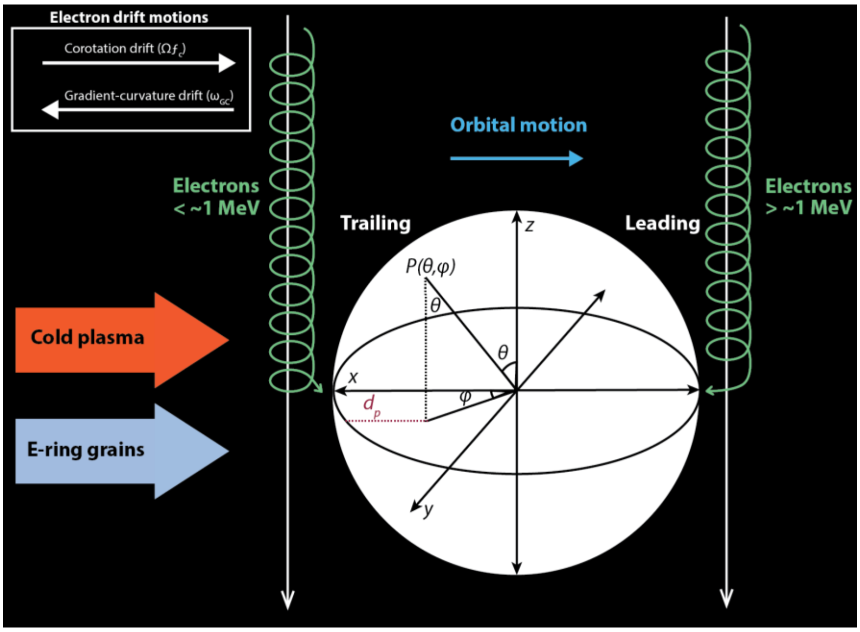

Figure 1 – Illustration of exogenic weathering factors at Mimas. Energetic electrons below the resonance energy of ~1 MeV preferentially bombard the trailing hemisphere, while electrons above this energy preferentially bombard the leading hemisphere. Cold plasma ions and electrons as well as E-ring dust grains preferentially bombard the trailing hemisphere. Not shown are interplanetary dust particles and energetic ions, which are expected to bombard the surface roughly uniformly. Superimposed is an illustration of the projected distance in the equatorial plane of Mimas, d_p, for a point P(θ, φ) on the surface (after Patterson et al. 2012).

As their gyro-radii are small relative to the moon and their bounce motion is generally much faster than their drift across the disk of the moon, energetic electrons will be absorbed by the surface almost immediately once their guiding centers come close enough to the moon's surface. However, the ratio between bounce and drift speeds depends on the electron energy, and thus electrons can reach different surface locations depending on their energies (as well as pitch angle and gyrophase). The bounce-averaged longitudinal distance (expressed as a fraction of the moon radius) that the electron of a given energy E and magnetic mirror latitude λ_m can travel across the disk of the moon before it is absorbed can be given by,

$$d\left(E,\lambda_m\right)=\omega L\left(\frac{t_b\left(E,\lambda_m\right)}{2}\right)\left(\frac{R_{Saturn}}{R_{Moon}}\right)$$

where ω is the particle's net azimuthal drift rate around Saturn, L is the dimensionless L-shell at the location of the moon, t_b is the particle's bounce time between magnetic mirror points and R_{Saturn} and R_{Moon} are the radii of Saturn and the moon, respectively. The L shell parameter equals the distance from the planet's center to the point where a given magnetic field line intersects the magnetic equator. The azimuthal drift rate is given by

$$\omega = f_c\left(L\right)\Omega_{Saturn}+\omega_{GC}\left(L,E,\lambda_m\right)-\omega_{Moon}$$

where Ω_{Saturn} is the rotation rate of Saturn, $f_c\left(L\right)$ represents the corotation fraction at the moon's L-shell, ω_{GC} is the gradient-curvature drift rate in the corotating frame of Saturn and ω_{Moon} is the angular rate of the moon's motion around Saturn in inertial space. The bounce time t_b and the gradient-curvature drift rate ω_{Drift} are calculated following the method of Thomsen and Van Allen (1980), which assumes a dipole magnetic field. As the longitudinal speed due to gradient-curvature drift increases relative to the bounce speed, more energetic electrons will, on average, be capable of drifting further across the disk of the moon before a bounce intersects the surface. Thus, at the leading hemisphere, electrons near the keplerian resonance energy only have access to a narrow region near the moon's equator, whereas higher energy electrons are capable of bombarding higher latitudes. For the trailing hemisphere, lower energy electrons have access to a larger range of latitudes, while the electrons with energies just below the resonance energy are confined to a narrow region near the equator. This is the basis for the lens-like electron bombardment pattern, which has been studied extensively for both Europa (Paranicas et al., 2001; Patterson et al., 2012) and Saturn's moons (Paranicas et al., 2012, 2014; Schenk et al., 2011).

Field Code Changed

To estimate whether an electron of a given energy can impact a point on the surface, we carry out a calculation in the idealized case. For a given point (θ, φ) on the surface, we may calculate a projected distance from the equatorial plane of the moon:

$$d_p = R_{moon}\left(1+\sin^2\theta(\cos^2\varphi-\sin^2\varphi)-2\sin\theta\cos\varphi(1-\sin^2\theta\sin^2\varphi)^{1/2}\right)^{1/2}$$

where θ is the colatitude and φ is an azimuthal angle measured clockwise from the direction into the co-rotational plasma flow (a similar formula was printed incorrectly in Patterson et al. 2012). If an electron with a given E and λ_m has $d(E, \lambda_m) \geq d_p$, both given in fraction of moon radius, it may in principle have access to that point P(θ, φ) on the moon's surface. Thus, we use this method to evaluate which part of the electron energy spectrum (and pitch angle distribution) has access to the surface for a given location on the moon. The energetic electrons in the inner magnetosphere of Saturn have a "pancake" pitch angle distribution centered around an equatorial pitch angle of ~ 90°(Carbary et al., 2011). If we integrate this distribution over all pitch angles, the mean equatorial pitch angle will typically be ~50° - 60°. For the purposes of this study, we have assumed an equatorial pitch angle of 59°. This gives us an average sense of the electron bombardment at Mimas. Plasma is close to co-rotating with Saturn at Mimas's location in the inner magnetosphere (e.g. Livi et al. (2014) and references therein). Here we use a co-rotatation fraction $f_c(3.08)$ of 97% as given by Mauk et al. (2005). Under these conditions, the keplerian resonance energy is calculated to occur at 1.04 MeV.

Field Code Changed

At the relevant energies discussed here (e.g. <10 MeV), the electron gyroradius is only a small fraction of the moon radius and the use of the guiding center approximation is therefore reasonable. Furthermore, the method described above assumes that the saturnian magnetic field is dipolar, which is a reasonable assumption for the inner saturnian moons (e.g. Arridge et al., 2012). It should also be noted that the saturnian magnetic dipole is shifted slightly northward relative to the rotational equator (Dougherty et al., 2005), however this was deemed to have a minimal effect on our results. Furthermore, our method does not take into account any magnetic field deviations near the moon. While Mimas could possess a sputtered exosphere, this is not likely to be robust enough to support ionospheric currents that would cause a significant plasma interaction and thus perturbation to the magnetic environment near the moon (Saur and Strobel, 2005). Additionally, Paranicas et al. (2014) have shown that the inner saturnian moons would have to be magnetized to levels on the order of the background magnetic field strength before any significant deviation from the 'lens' bombardment pattern would be expected. Therefore, magnetic perturbations due to the presence of Mimas in the saturnian magnetosphere are unlikely to significantly affect our results.

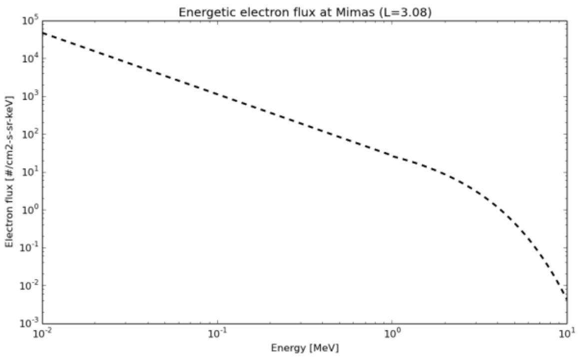

Figure 2 - Energetic electron spectrum at Mimas based on averaged measurements by the *Cassini* MIMI-LEMMS sensor at a narrow corridor near the orbit of Mimas (~3.08 R_s) during the period 2004 - 2013. The onset of a macrosignature is known to occur near 10 MeV(Paranicas et al., 2014; Selesnick, 1993). For the purposes of this study we therefore assume zero flux above this energy.

The electron spectrum at the orbit of Mimas was implemented according to the fit functions provided by Paranicas et al. (2014), where the form $\log_{10} j = m\log_{10} E + b$ was used below 962 keV and the form $j = j_0 E^a \exp(-E / E_0)$ was used at higher energies. Here E represents the electron energy in MeV, j is the directional differential electron flux in units of particles cm^{-2} s^{-1} sr^{-1} keV^{-1}, and the fit parameters m=−1.62, b=1.43, j_0=63.1, E_0=1.12 and a=−0.3 are from Paranicas et al. (2014). These fit parameters were based on averaged measurements from the *Cassini* Magnetosphere Imaging Instrument (MIMI) Low Energy Magnetospheric Measurement System (LEMMS) (Krimigis et al., 2004) in a narrow corridor near the orbit of Mimas (~3.08 R_s) during the period 2004 - 2013. Previous studies have found a persistent electron flux depletion, sometimes referred to as a macrosignature, near the orbit of Mimas beginning at an energy between 7 - 17 MeV (Selesnick, 1993).

This is due to the fact that electrons at and above these energies drift around Saturn rapidly, frequently re-encounter Mimas and are absorbed. For these electrons, virtually no stable flux builds up along Mimas's orbit. Similar proton macrosignatures can be observed at energies as low as a few hundred keV near Mimas (Kollmann et al., 2013). Based on the characteristics of the LEMMS measurements and physical arguments, Paranicas et al. (2014) chose an energy onset for the Mimas electron macrosignature of 10 MeV. Following that work, we assume that the flux above 10 MeV is at levels common in such a macrosignature and therefore negligible. We thus populate the energetic electron spectrum from 10 keV up to 10 MeV. The resulting Mimas electron spectrum is shown in Figure 2.

The interaction of electrons with the surface of Mimas was implemented using the PLANETOCOSMICS code (http://cosray.unibe.ch/~laurent/planetocosmics/) (Desorgher et al., 2005), which is based on the Geant4 Monte Carlo simulation toolkit for particle interactions with matter (Agostinelli et al., 2003). This code handles both nuclear and electromagnetic interactions of primary and secondary particles with matter, including secondary electron production and the production of bremsstrahlung photons. Additionally, the Geant4 toolkit provides a set of extensions for low-energy electromagnetic physics (Chauvie et al., 2004) that were utilized for the work described herein. The simulation geometry was constructed as a flat slab of H_2O with a density of 1 g cm^{-3}. The flux of incident electrons was simulated by a point source located above the surface and delivered with a cosine law angular distribution in order to capture the effects of electrons that are not incident on the surface along or close to the direction of the normal. This is an appropriate representation, as a gyrotropic distribution with near-equatorial pitch angles will bombard the surface with roughly isotropic incidence angles (e.g. Paranicas et al. 2009).The energy deposited by all primary and secondary particle interactions within the surface geometry layer was recorded at 1 µm depth intervals.

The model was constructed such that the surface of Mimas was divided into a grid of 800 latitude/longitude bins. The electron cutoff energy E_c was calculated by solving $d(E_c)=d_p(\theta, \varphi)$ for E_c at each point $P(\theta, \varphi)$ on the surface of Mimas. For the trailing hemisphere, E_c represents the highest energy electrons (below the Keplerian resonance energy) that have access to that surface location. For the leading hemisphere, E_c represents the lowest energy electrons (above the Keplerian resonance energy) that have access to that surface location.

Using the appropriate electron cutoff energy, the electron spectrum was then populated according to the fit functions given above and a PLANETOCOSMICS simulation executed for this primary particle spectrum. The results for each individual PLANETOCOSMICS simulation was stored along with the corresponding latitude/longitude bin and assembled to create a global map of energetic electron dose versus depth. The resulting global maps are presented, overlaid onto a cylindrically projected basemap of Mimas.

2. Results

3.1 – Energetic electron bombardment patterns

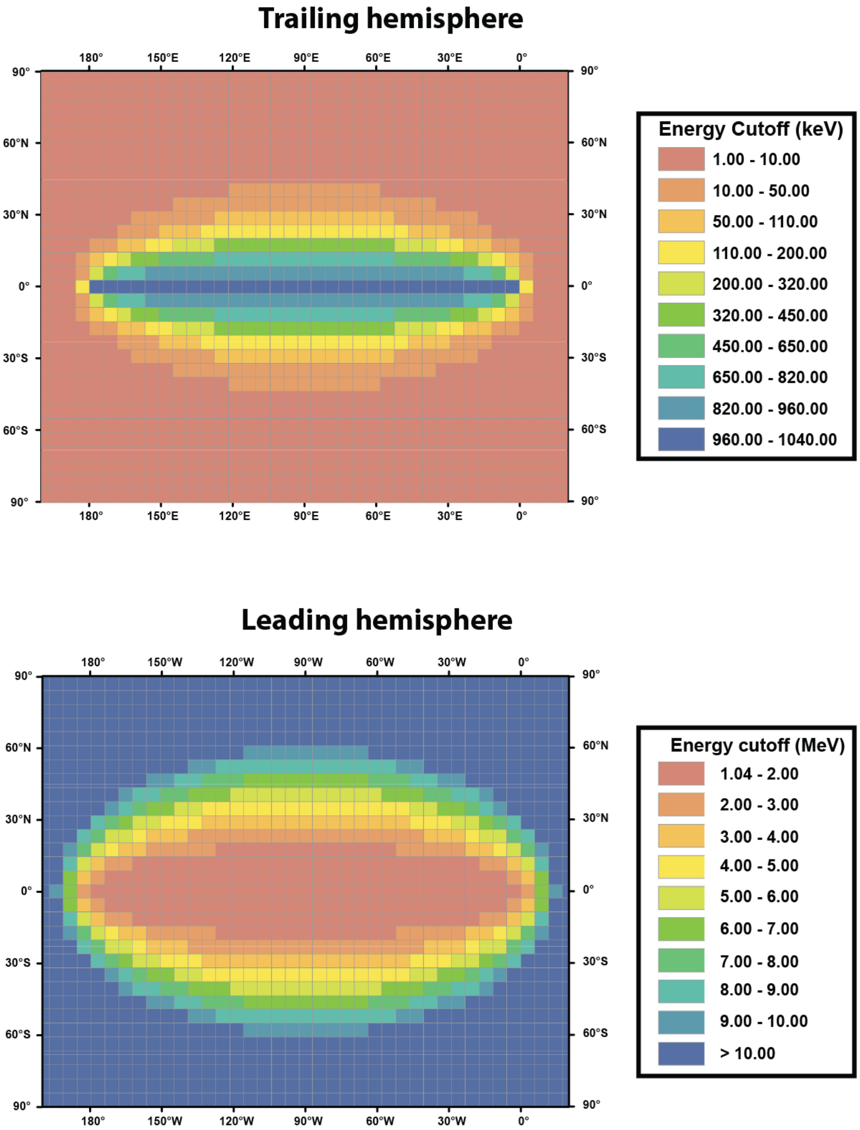

Figure 3 – Predicted cutoff energy versus surface location for Mimas. On the trailing hemisphere (top), the cutoff energy represents the highest energy electrons capable of accessing that point on the surface. On the leading hemisphere (bottom), the cutoff energy represents the lowest energy electrons capable of accessing that point. Map projection is simple cylindrical.

Shown in Figure 3 are the calculated electron cutoff energies for different surface locations based on the bounce averaged approach described in section 1. For the trailing hemisphere, the electron energy cutoff represents the highest energy electrons capable of accessing a given surface location. At the trailing hemisphere apex (90° E) energetic electrons with E > 10 keV have access to a region which is within ± 43° of the equator. Electrons with energies in the 100 keV range are only capable of reaching a relatively narrow region of ± 27° at the apex, while the most energetic electrons near the resonance energy at ~1 MeV only have access to a narrow region near at the equator. Paranicas et al. (2014) focused almost exclusively on the leading hemisphere bombardment, so these are the first ever calculations of the trailing hemisphere electron contours for Mimas.

For the leading hemisphere, the electron energy cutoff value represents the lowest energy electrons that have access to a given surface location. Thus, the narrow region within ± ~20° of the equator at the leading hemisphere apex (90° W) is bombarded by electrons near the resonance energy of 1.04 MeV up to 10 MeV. In comparison, at ± ~50° near the leading apex, only electrons with E > 7 MeV are capable of bombarding the surface. High-latitude regions (e.g. above 60° near the leading apex) are only accessible to electrons with E > 10 MeV. If we assume that the energetic electron macrosignature starts at ~10 MeV, this implies that these high-latitude regions are minimally affected by energetic electrons from the saturnian magnetosphere.

3.2 Energy deposition at depth

In order to relate the energy deposited at depth within the surface to a dose, we have calculated the energy deposition in terms of time to reach a dose of 100 eV per 16 amu of surface material (equivalent to 100 eV per Oxygen atom). This unit is commonly used for theoretical and laboratory studies of irradiated ices and represents a chemically significant dose where most bonds are broken at least once (Cooper et al., 2001; Hand and Carlson, 2012, 2011; Johnson et al., 2004; Paranicas et al., 2009). Thus, although we do not precisely know the thresholds for the physical processes involved in modification of surface material (e.g. grain sintering, production of voids and defects), we use this quantity as a proxy for significant chemical or physical alteration of surface material. Shown in Figures 4 and 5 is the time to reach this chemically significant dose at several different depths within the subsurface of Mimas.

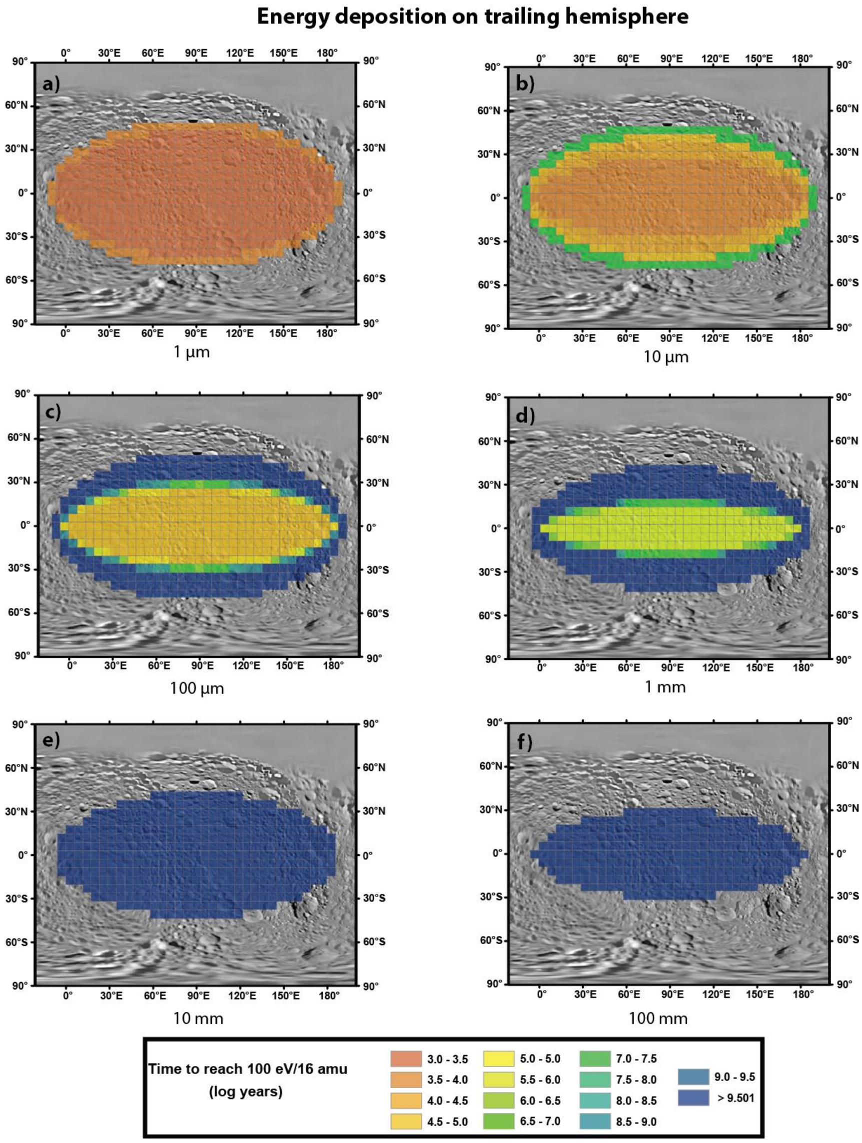

Figure 4 - Energy deposition maps at different depths on the trailing hemisphere of Mimas. The energetic electron dose is given in terms of years to reach a significant dose of 100 eV/ 16 amu, which is equal to a dose of 60.3 Grad. Map projection is simple cyclindrical.

As shown in Figure 4 a) and b), a large fraction of the trailing hemisphere surface reaches a significant dose within timescales of 10^3 – $10^{4.5}$ years at depths of 1 -10 µm.

At a depth of 100 µm (Figure 4 c), a narrow band within ± ~25° of the equator at the trailing hemisphere will reach a significant dose on timescales of $10^{4.5}$ – $10^{5.0}$ years, while the dose at higher and lower-latitude locations is negligible. At 1 mm (Figure 4 d) depths, the equatorial lens has shrunk to a narrow band that extends to ± ~15° of the equator near the trailing hemisphere apex, reaching a significant dose on timescales of $10^{5.5}$ – $10^{6.0}$ years. While a significant dose may be reached on timescales of $10^{6.0}$ – $10^{7.5}$ years around the edges of the narrow equatorial lens, latitudes beyond ± ~20° degrees at the trailing hemisphere apex receives a negligible energetic electron dose and is therefore not likely to be heavily processed. As shown in Figure 4 e) the trailing hemisphere does not receive any significant energetic electron dose at centimeter depths.

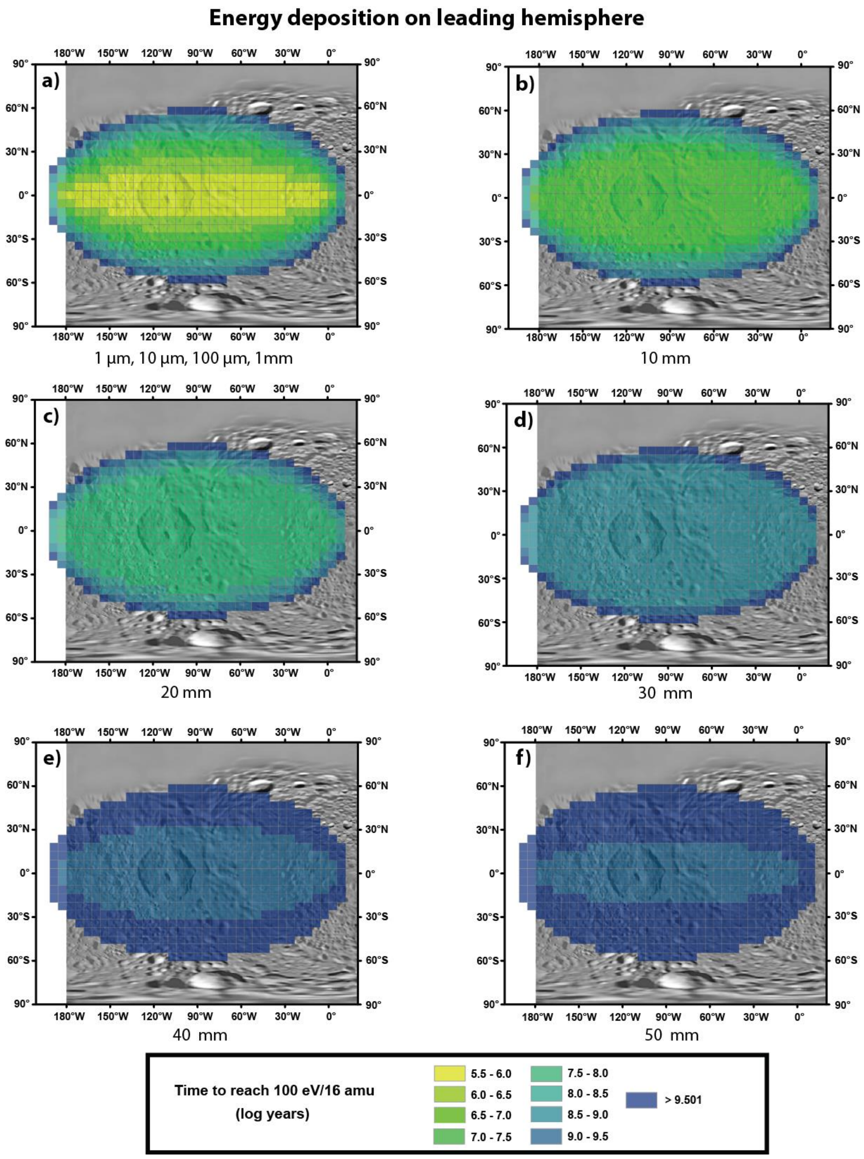

Figure 5 - Energy deposition maps on different depths at the leading hemisphere of Mimas. The energetic electron dose is given in terms of years to reach a significant dose of 100 eV/ 16 amu, which is equal to a dose of 60.3 Grad. Map projection is simple cylindrical.

Because the > 1 MeV electrons precipitating into the leading hemisphere tend to reach much larger depths, in these plots we show five examples of depths in the one to several cm range. As shown in Figure 5 a) and b), the leading hemisphere surface at low latitudes near the apex (within ± 15°) receives a significant dose on timescales of

$10^{5.5}$ – $10^{6.0}$ years, while higher latitude regions within ± 45° near the apex reach this dose level on timescales of $10^{6.0}$ – $10^{8.0}$ years. As shown in Figure 5 a), the timescales for modification and the lens deposition pattern remain unchanged until ~ mm depths into the subsurface are reached. At 10 mm depths (Figure 5 b), the narrow near-equatorial enhancement (due to the ~1 MeV electrons) is no longer present and modification timescales are $10^{6.5}$ – $10^{7.5}$ years for a large region, which is ± ~40° of the leading hemisphere apex. At 20 mm depths (Figure 5 c), modification timescales are $10^{7.5}$ – $10^{8.5}$ years within ± ~50° of the leading hemisphere apex. At 30 mm depths (Figure 5 d), the modification timescales are $10^{7.5}$ – $10^{8.5}$ years within the same area latitude range ± ~50°. At depths of 40 mm and greater (Figure 5 e), the energetic electron dose is negligible and the modification timescales are > 10^9 years everywhere within a large lens region which is ± ~60° of the leading hemisphere apex.

4. Discussion

Here we have modeled the interaction of energetic electrons with surface material on Saturn's inner mid-sized moon Mimas, showing that the electron dose is primarily concentrated in low-latitude lens-shaped regions on both the leading and trailing hemispheres. We have shown that on the trailing hemisphere, the uppermost 10 µm of the surface within the lens region reaches a significant dose of 100 eV/16 amu on timescales of 10^3-10^4 years. At larger depths the lens-like region shrinks as only the most energetic electrons with the highest penetration range into the ice are capable of reaching these layers. At 1 mm, the lens-shaped region extends to ± ~15° of the equator near the trailing hemisphere apex and the timescales for reaching a significant dose are $10^{5.5}$ – $10^{6.0}$ years. Beyond ~a few mm however, the energetic electron dose drops off very steeply, and at 10 mm depths the dose is negligible. This is consistent with the fact that the highest energy (~1 MeV) electrons at the trailing hemisphere have a mean range of < 5 mm into the surface (Berger et al., 2005).

On the leading hemisphere surface, a narrow lens-shaped region ± ~15° of the equator near the apex reaches a significant dose of 100eV/16 amu on timescales of $10^{5.5}$ – $10^{6.0}$ years, while surrounding regions reach this dose level on timescales of $10^{6.0}$ – $10^{8.0}$ years. This electron deposition pattern and dose level remains unchanged until ~ 10 mm depths are reached, after which the dose is more uniformly distributed across a large lens-shaped region within ± 40-50° of the equator at the apex, with timescales of $10^{6.5} – 10^{8.5}$ years to reach a significant dose. At greater than ~40 mm depths, the electron dose within the lens-shaped region is negligible, with modification timescales of $>10^9$ years. This is consistent with the fact that the electron flux spectrum drops off rapidly with increasing energy (c.f. Figure 2). Therefore, as the lowest energy electrons near the resonance energy of ~1 MeV reach their maximum range into the surface, the electron dose drops off rapidly with increasing depth. The highest energy electrons at 10 MeV have a mean range into the surface ice of < 50 mm (Berger et al., 2005), and therefore the dose at greater depths is primarily the result of secondary bremsstrahlung photons. At Jupiter's moon Europa, Paranicas et al. (2009) found that secondary bremsstrahlung radiation leads to a significant dose down to meter depths. However, our results show that this is not the case at Mimas, where energetic electron fluxes are much lower and the spectrum effectively only extends up to energies of ~10 MeV.

While the present work models only the effect of energetic electrons, Mimas is also exposed to several other charged particle weathering agents. The moon orbits inside the cold dense plasma of Saturn's inner magnetosphere, with typical ion and electron temperatures of 20 eV and 1 eV, respectively (Roussos et al., 2010). At such low energies, electrons and ions have a range into the surface of < 1 µm and can therefore be neglected when discussing radiation dose at greater depths. Similarly, only energetic electrons with energies > 10 keV have a range into the surface that exceeds a few µm. Saturn also hosts populations of energetic ions, however, many ions (e.g. protons below about 100 keV) are readily lost via charge exchange interactions with neutrals and are therefore heavily depleted in the neutral-rich inner magnetosphere where Mimas resides (Andre et al., 2008; Paranicas et al., 2012; Young et al., 2005). Additionally, protons above a few hundred keV are present only at very low fluxes along Mimas's orbit due to macrosignature formation. More importantly, however, is the fact that since energetic ions have large gyroradii and long bounce times, their bombardment pattern across the surface of Mimas will be more globally uniform compared with the significant spatial non-uniformity expected for bombardment by energetic electrons. To determine an upper limit on the effects of proton bombardment at Mimas we have used the energetic proton flux spectrum at L=3.08 from Paranicas et al. (2012) and PLANETOCOSMICS to calculate a dose-depth curve that should be approximately valid for all surface locations (Figure 6). The Paranicas et al. (2012) proton fluxes represent the proton environment inside the narrow sweeping corridor along the orbit of Mimas. At the leading hemisphere, the dose due to protons is comparable to the electron dose in the uppermost ~few µm. However, the proton dose drops of rapidly with depth and is over a magnitude lower than that of the electrons at 20 - 30 µm at the apex of the leading hemisphere. As we have shown here, the radiation dose due to energetic electrons is significantly reduced as we move away from the lens-shaped regions near the equator. Depending on surface location, energetic protons may therefore contribute a non-negligible fraction of the overall dose at shallower depths (< 30 µm), particularly at high latitudes. The contribution from the proton dose at larger depths is very small at all surface locations.

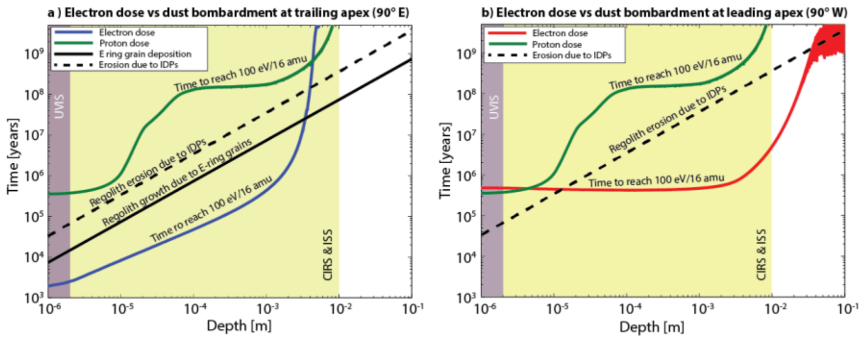

Figure 6 - Timescales for energetic electron dose accumulation at a given depth compared to time that it takes for the surface regolith to be modified to that depth due to dust deposition for a) the trailing hemisphere apex and b) the leading hemisphere apex. The energetic proton dose assuming isotropic bombardment is also shown for comparison. Also shown are approximate sampling depths for UVIS, CIRS and ISS from Hendrix et al. (2012). For CIRS the sampling depth is given by the thermal skin depth. It should be noted that exact sampling depths for these instruments will depend on local surface properties.

In addition to weathering by charged particles, the surface of Mimas is also exposed to several populations of in-falling dust grains. The most significant source of these is the E-ring, which consists of dust grains produced by outgassing at the moon Enceladus (Kempf et al., 2010, 2008; Postberg et al., 2008). Once ejected, E-ring grains experience motion due to gravity, solar radiation pressure and electromagnetic forces in Saturn’s magnetosphere (Hamilton and Burns, 1994; Horanyi et al., 1992; Horányi et al., 2008). Based on studies that have performed dynamical modelling of grain trajectories, it is expected that E-ring grains will primarily deposit onto the trailing hemisphere of Mimas (Hamilton and Burns, 1994), with the highest dust flux expected at the center of the trailing hemisphere (Juhász and Horanyi, 2015). Deposition of E-ring grains will lead to a growth of the surface regolith on Mimas over time, possibly presenting an effect that competes with charged particle modification and UV photolysis of surface material. If the regolith growth is sufficiently fast, surface material at a given depth would not have sufficient time to undergo significant charged particle processing before it is buried. Using an estimated E-ring dust flux of 4.3 x 10^{-12} g m^{-2} s^{-1} (Juhász and Horanyi, 2015), and assuming a density of 1 g cm^{-3} we have calculated the regolith growth due to E-ring grain deposition at the trailing hemisphere apex, where the E-ring flux is expected to be greatest. Shown in Figure 6 is a comparison of the energetic electron dose at a given depth versus the time it takes for the regolith to be modified to the same depth by dust grain deposition onto the surface. As can be seen, the timescales of electron dose accumulation are much faster than E-ring grain deposition for depths < 1 mm at the trailing hemisphere apex. Beyond this depth regolith modification due to the deposition of E-ring grains begins to dominate. At the trailing hemisphere, radiation processing is therefore expected to be a significant modification process only down to ~ 1 mm depths. It is also expected that gas-phase neutrals from the extended Enceladus neutral cloud will deposit onto the surfaces of the inner satellites (Cassidy and Johnson, 2010; Jurac and Richardson, 2007). Cassidy and Johnson (2010) estimated that these neutrals are deposited primarily at the trailing hemisphere of Mimas at rates comparable to, but slightly higher than, the flux of E-ring grains predicted by Juhasz and Horanyi (2015). In addition to E-ring grains and gas-phase neutrals, the surface of Mimas is exposed to dust deposition by interplanetary dust particles (IDPs), which originate primarily from four sources: Jupiter-family comets, Halley-type comets, Oort-Cloud comets, and Edgeworth-Kuiper Belt objects (Poppe, 2016). It should be noted that dust impact onto the surface may also lead to surface erosion and production of dust ejecta (Krivov et al., 2003; Spahn et al., 2006), particularly in the case of the IDPs, which have high velocities relative to the saturnian moons (Poppe, 2016; Porter et al., 2010). For Mimas, Spahn et al. (2006) estimated that the mass flux of escaping ejecta resulting from IDP bombardment is on the order of ~10^2 higher than the incoming IDP mass flux to the surface. This implies that IDP bombardment leads to a net loss of surface material and erosion of the surface. The exact manner by which the surface is modified by bombardment from high velocity IDPs is not entirely clear and depends to some extent on the mechanical properties and physical state of the surface (e.g. fluffy regolith versus a solid surface) (Porter et al., 2010; Spahn et al., 2006). Nonetheless, for the purpose of a comparison with our electron irradiation results, we have made a rough estimate of the surface erosion rate over time due to IDPs based on the mass flux ratio from Spahn et al. (2006). Based on measurements of IDPs in the inner solar system we assume a density for these particles of 2.5 g cm^{-3} (Jessberger et al., 2001). To first order we assume that IDPs bombard the surface more or less isotropically and use the free-space IDP flux at the orbit of Mimas from Poppe (2016) of ~4.0 x 10^{-14} g m^{-2} s^{-1}. As shown in Figure 6 a), the regolith growth due to dust deposition by E-ring grains dominates over erosion due to bombardment of IDPs at the trailing hemisphere. The leading hemisphere of Mimas is not expected to be heavily bombarded by E-ring grains, and at the apex of the leading hemisphere the flux of E-ring grains is expected to be roughly zero (Juhász and Horanyi, 2015). IDP bombardment is therefore expected to be the primary competing process to electron irradiation over much of the leading hemisphere. As shown in Figure 6 b), IDP bombardment may be a competitive process within the upper ~10 µm of the surface. However, at depth the effect of IDP deposition onto the leading hemisphere of Mimas is negligible compared to the more rapid weathering of the surface due to energetic electron bombardment. While interstellar dust particles may in principle also contribute to surface modification, the flux of these particles is several orders of magnitude lower than the IDP flux at Saturn (e.g. Altobelli et al., 2016) and can therefore be considered to be negligible in this context.

Finally, Mimas is also exposed to weathering by UV photons. Using observations by the *Cassini* UVIS instrument, Hendrix et al. (2012) studied the surface of Mimas at far-ultraviolet wavelengths (170 – 190 nm) and noted a generally lower albedo than expected for a water ice surface, with latitudinal variations consistent with enhanced photolytic production of H_2O_2, a known UV darkening agent (Carlson et al., 1999), during southern summer. At far-ultraviolet wavelengths UVIS is sampling the uppermost ~ µm of the surface, where the effects of cold plasma bombardment, neutrals (dust and gas) and weathering by photolysis are expected to be dominant over those of energetic electron bombardment. However, Hendrix et al. (2012) also noted what could be a faint signature of one of the leading hemisphere-lens ansae in the far-ultraviolet observations, which may be due to enhanced production of H_2O_2 there by energetic electrons. Our model results show that a significant energetic electron dose is deposited at shallow (~ µm) depths. Furthermore, we also note that the leading and trailing hemisphere lenses have some overlap near 180° longitude, which leads to an increased electron dose near the ansae of the leading hemisphere lens at shallow (<100 µm) depths. This is consistent with enhanced radiolytic production of H_2O_2 as suggested by Hendrix et al. (2012).

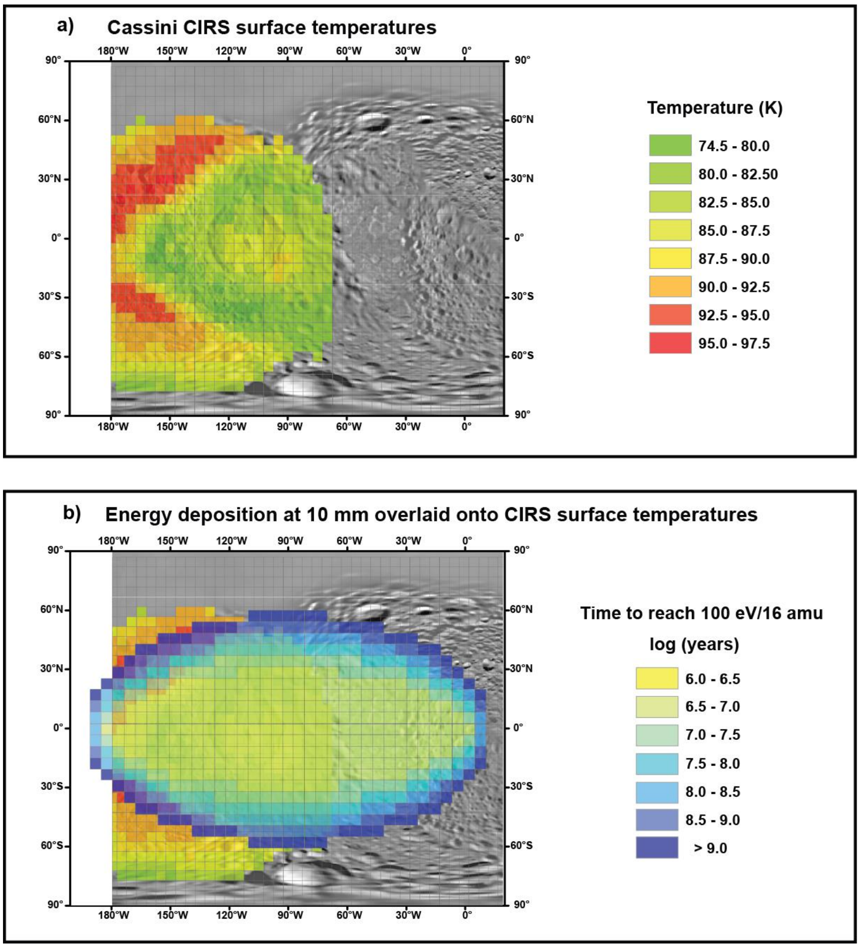

Figure 7 - a) Daytime surface temperature derived from CIRS observations taken on 13 February 2010 (orbit 126), b) overlaid by the calculated energy deposition at 10 mm depth from our model. Map projection is simple cylindrical.

The calculated dose-depth profiles for the leading hemisphere are consistent with the observation of lens-shaped equatorial anomalies by the ISS (Schenk et al., 2011), CIRS (Howett et al., 2011) and VIMS (Filacchione et al., 2016) instruments. The

CIRS instrument observed diurnal temperature variations that are sensitive to surface thermophysical properties over a depth range determined by the thermal skin depth, which is the depth to which the diurnal wave penetrates. Howett et al. (2011) estimated a thermal skin depth inside the lens-shaped region of 1.31 – 2.71 cm, consistent with our results, which indicates that the surface is heavily processed down to depths of ~30 mm inside this region. Shown in Figure 7 are daytime temperature observations derived from CIRS observations overlaid by the calculated energy deposition pattern at a depth of 10 mm from our model. Howett et al. (2011) proposed that energetic electrons may alter the bulk thermal properties of surface material, leading to the thermal inertia anomaly observed by CIRS. Recently, Schaible et al. (2016) showed results of molecular dynamics simulations that confirm that grain sintering by energetic electrons can affect thermal conductivity of surface material over realistic timescales. This is explained by molecular motion resulting from ionization of molecules in the surface material, ultimately leading to modification of contact boundaries between individual grains. These authors note that more detailed modeling is required to fully characterize and quantify this process and thus it is difficult to perform a direct comparison between our energy deposition maps and the observed thermal inertia values. However, as shown in Figure 7 b) we observe that the sharp boundaries of the lens-shaped region in the CIRS daytime temperature map are a remarkably close match to boundaries in our energy deposition map at 10 mm. Similarly, the ISS color anomaly is observed as enhanced scattering at a wavelength of 338 nm (Schenk et al., 2011), at which the ISS observations are sensitive to the uppermost ~cm of the surface (Hendrix et al., 2012). This is consistent with our findings of significant energetic electron processing of surface material down to ~cm depths on the leading hemisphere. The amount of time required to form the observed thermal anomaly will depend on the electron sintering timescales, which in turn depend strongly on physical properties of surface material, such as the grain size, shape and degree of compaction (Schaible et al., 2016). These parameters are currently not strongly constrained for the surface of Mimas (e.g. Ferrari and Lucas, 2016). Our results show that it takes ~10^6 years to reach a dose of 100eV/16 amu inside the lens at ~cm depths. At this radiation dose level, each molecule of surface material will, on average, have been ionized several times. It is therefore reasonable to assume that this may be taken as an upper limit for the time it takes to form the lens-shaped thermal anomaly at Mimas.

Our calculated dose-depth maps for the trailing hemisphere indicate the presence of a lens-shaped electron bombardment region centered on the equator, which is somewhat narrower in latitudinal extent than the leading hemisphere lens. Our results also show that the radiation processing timescales within the upper ~mm of the surface are significantly shorter at the trailing hemisphere lens (c.f. Figure 6). However, no corresponding trailing hemisphere lens feature has to date been observed by the *Cassini* remote sensing instruments. In the case of CIRS this may be due to the fact that the thermal skin depth at the trailing hemisphere is expected to be on the order of ~cm (Howett et al., 2011) and our results indicate that the electron dose is only significant down to ~mm depths. Thus it is possible that while electron sintering may indeed be occurring within the upper ~mm of the trailing hemisphere lens, it does not result in significant thermophysical alteration to the bulk of the material sampled by the diurnal wave, and subsequently no anomalous surface temperatures are observed by CIRS. However, it should be noted that the CIRS observational coverage at Mimas's trailing hemisphere is limited, which complicates the search for a thermal anomaly there. The Mimas surface temperature maps of Filacchione et al. (2016) do not have observational coverage at the trailing hemisphere, however we expect that VIMS, like CIRS, might be similarly unable to sense anomalous surface temperatures due to the trailing hemisphere lens. A similar argument may apply to observations by ISS, where enhanced production of ice defects due to energetic electrons in the uppermost layer is too shallow to affect the bulk scattering properties of the volume of surface material that is sampled. The UVIS instrument, however, may in principle be capable of observing the trailing hemisphere lens in the far-ultraviolet, which senses the uppermost ~ µm of the surface (Hendrix et al., 2012). We have shown that dose accumulation timescales at the center of the low-latitude trailing hemisphere are comparatively short (< 10^4 years), faster than the expected regolith growth due to deposition of E-ring grains. However, the trailing hemisphere is also exposed to bombardment by cold co-rotational plasma, which results in an observed reddening of the trailing hemisphere by ISS (Schenk et al., 2011) and a possible darkening in the same location by UVIS (Hendrix et al., 2012). This cold plasma leads to the regular addition of electrons, protons, and water group ions to the top ~1 µm of the surface, the same depths sensed by UVIS, and the cold plasma bombardment pattern extends to ~ ±90° in latitude over the trailing hemisphere (e.g. Figure 3 in Schenk et al.

(2011)). It is therefore plausible that the effect of plasma bombardment is effectively obscuring the trailing hemisphere lens at the shallow depths sensed by UVIS. However, it should be noted that, as is the case with CIRS, the UVIS coverage of Mimas' trailing hemisphere is similarly limited.

5. Summary

We have produced for the first time both leading and trailing hemisphere dose versus depth maps for energetic electron bombardment of Saturn's innermost mid-sized moon Mimas using a combination of particle tracing and modeling of electron interactions with surface ice using a particle physics code. Our results are consistent with observations of a leading hemisphere lens-shaped anomaly by the ISS, CIRS, VIMS and UVIS instruments on-board the *Cassini* spacecraft, and we have demonstrated the importance of accurate knowledge of dose versus depth into the surface for comparisons to remote sensing observations. We estimate an upper limit of ~10^6 years for the time required to form the observed leading hemisphere lens. While our results also predict a lens-shaped energetic electron bombardment pattern on the trailing hemisphere, no such region has yet been observed by the *Cassini* remote sensing instruments. We suggest that the lack of detection of such a feature in the CIRS and ISS observations is likely due to the shallower penetration depth of the prograde (< 1.04 MeV) electrons that preferentially bombard the trailing hemisphere. The trailing hemisphere is also the main hemisphere for other processes (e. g. deposition of E ring material and corotating plasma) as discussed above. For observations by the UVIS instrument, which samples the uppermost layers of the surface, we suggest that bombardment by cold plasma is obscuring the effect of the energetic electron lens. This may therefore be an example of a case where we cannot directly observe certain surface properties using Cassini's remote sensing instruments but may predict them by using a combination of observations from its in-situ instruments (in this case MIMI-LEMMS) and modeling.

For both hemispheres our results indicate that the uppermost surface consists of a layer of material that's been significantly processed by energetic electrons. Several mechanisms have been proposed for how energetic electrons modify the surface material of icy moons and how this modification relates to remote sensing observations. These include production of defects in surface ice that act to increase scattering of photons at certain wavelengths (Schenk et al., 2011), sintering of ice grains on the surface that leads to enhanced thermal conductivity (Howett et al., 2012a, 2012b, 2011; Schaible et al., 2016), and production of radiolytic products such as H_2O_2, a known UV darkening agent (Hendrix et al., 2012). However, these processes have to date not been explicitly modelled for realistic conditions at Saturn's icy moons and a quantitative comparison between remote sensing observations and charged particle modification has therefore not been possible. Mimas, which is heavily irradiated by energetic electrons and exposed to significant dust bombardment by E-ring grains is an ideal subject for studies of space weathering effects at airless bodies within planetary magnetospheres. The spatially resolved dose versus depth-profiles presented herein therefore serve as a basis for future studies of energetic electron weathering in the Saturn system.

Acknowledgements

This research was supported by an appointment to the NASA Postdoctoral Program at the Jet Propulsion Laboratory administered by Oak Ridge Associated Universities and Universities Space Research Association through a contract with the National Aeronautics and Space Administration (NASA). K. P. Hand acknowledges support from the Jet Propulsion Laboratory, California Institute of Technology, under a contract with the NASA. C. Howett would like to thank the NASA Cassini Data Analysis program, which partly funded this work (NNX12AC23G). AJC and GHJ acknowledge support by the UK Science and Technology Facilities Council.

References

Agostinelli, S., Allison, J., Amako, K., Apostolakis, J., Araujo, H., Arce, P., Asai, M., Axen, D., Banerjee, S., Barrand, G., Behner, F., Bellagamba, L., Boudreau, J., Broglia, L., Brunengo, a., Burkhardt, H., Chauvie, S., Chuma, J., Chytracek, R., Cooperman, G., Cosmo, G., Degtyarenko, P., Dell'Acqua, a., Depaola, G., Dietrich, D., Enami, R., Feliciello, a., Ferguson, C., Fesefeldt, H., Folger, G., Foppiano, F., Forti, a., Garelli, S., Giani, S., Giannitrapani, R., Gibin, D., Gómez Cadenas, J.J., González, I., Gracia Abril, G., Greeniaus, G., Greiner, W., Grichine, V., Grossheim, a., Guatelli, S., Gumplinger, P., Hamatsu, R., Hashimoto, K., Hasui, H., Heikkinen, a., Howard, a., Ivanchenko, V., Johnson, a., Jones, F.W., Kallenbach, J., Kanaya, N., Kawabata, M., Kawabata, Y., Kawaguti, M., Kelner, S., Kent, P., Kimura, a., Kodama, T., Kokoulin, R., Kossov, M., Kurashige, H., Lamanna, E., Lampén, T., Lara, V., Lefebure, V., Lei, F., Liendl, M., Lockman, W., Longo, F., Magni, S., Maire, M., Medernach, E., Minamimoto, K., Mora de Freitas, P., Morita, Y., Murakami, K., Nagamatu, M., Nartallo, R., Nieminen, P., Nishimura, T., Ohtsubo, K., Okamura, M., O'Neale, S., Oohata, Y., Paech, K., Perl, J., Pfeiffer, a., Pia, M.G., Ranjard, F., Rybin, a., Sadilov, S., Di Salvo, E., Santin, G., Sasaki, T., Savvas, N., Sawada, Y., Scherer, S., Sei, S., Sirotenko, V., Smith, D., Starkov, N., Stoecker, H., Sulkimo, J., Takahata, M., Tanaka, S., Tcherniaev, E., Safai Tehrani, E., Tropeano, M., Truscott, P., Uno, H., Urban, L., Urban, P., Verderi, M., Walkden, a., Wander, W., Weber, H., Wellisch, J.P., Wenaus, T., Williams, D.C., Wright, D., Yamada, T., Yoshida, H., Zschiesche, D., 2003. Geant4—a simulation toolkit. Nucl. Instruments Methods Phys. Res. Sect. A Accel. Spectrometers, Detect. Assoc. Equip. 506, 250–303. doi:10.1016/S0168-9002(03)01368-8

Altobelli, N., Postberg, F., Fiege, K., Trieloff, M., Kimura, H., Sterken, V.J., Hsu, H.-W., Hillier, J., Khawaja, N., Moragas-Klostermeyer, G., Blum, J., Burton, M., Srama, R., Kempf, S., Gruen, E., 2016. Flux and composition of interstellar dust at Saturn from Cassinis Cosmic Dust Analyzer. Science (80-.). 352, 312–318. doi:10.1126/science.aac6397

Andre, N., Blanc, M., Maurice, S., Schippers, P., Pallier, E., Gombosi, T.I., 2008. Identification of saturn's magnetospheric regions and associated plasma processes: Rev. Geophys. 46, 1–22. doi:10.1029/2007RG000238.1

Arridge, C.S., André, N., McAndrews, H.J., Bunce, E.J., Burger, M.H., Hansen, K.C., Hsu, H.-W., Johnson, R.E., Jones, G.H., Kempf, S., Khurana, K.K., Krupp, N., Kurth, W.S., Leisner, J.S., Paranicas, C., Roussos, E., Russell, C.T., Schippers, P., Sittler, E.C., Smith, H.T., Thomsen, M.F., Dougherty, M.K., 2012. Mapping Magnetospheric Equatorial Regions at Saturn from Cassini Prime Mission Observations, Space Science Reviews. doi:10.1007/s11214-011-9850-4

Berger, M.J., Coursey, J.S., Zucker, M.A., Chang, J., 2005. ESTAR, PSTAR, and ASTAR: Computer Programs for Calculating Stopping-Power and Range Tables for Electrons, Protons, and Helium Ions (version 1.2.3).

Brown, R.H., Baines, K.H., Bellucci, G., Bibring, J.P., Buratti, B.J., Capaccioni, F., Cerroni, P., Clark, R.N., Coradini, A., Cruikshank, D.P., Drossart, P., Formisano, V., Jaumann, R., Langevin, Y., Matson, D.L., Mccord, T.B., Mennella, V., Miller, E., Nelson, R.M., Nicholson, P.D., Sicardy, B., Sotin, C., 2005. The Cassini visual and infrared mapping spectrometer (VIMS) investigation. Space Sci. Rev. 115, 111–168. doi:10.1007/s11214-004-1453-x

Buratti, B.J., Mosher, J.A., Johnson, T. V., 1990. Albedo and color maps of the Saturnian satellites. Icarus 87, 339–357. doi:10.1016/0019-1035(90)90138-Y

Carbary, J.F., Mitchell, D.G., Paranicas, C., Roelof, E.C., Krimigis, S.M., Krupp, N., Khurana, K., Dougherty, M., 2011. Pitch angle distributions of energetic electrons at Saturn. J. Geophys. Res. Sp. Phys. 116, 1–11. doi:10.1029/2010JA015987

Carlson, R.W., Anderson, M.S., Johnson, R.E., Smythe, W.D., Hendrix, A.R., Barth, C.A., Soderblom, L. a, Hansen, G.B., McCord, T.B., Dalton, J.B., Clark, R.N., Shirley, J.H., Ocampo, a C., Matson, D.L., 1999. Hydrogen peroxide on the surface of Europa. Science 283, 2062–4.

Cassidy, T.A., Johnson, R.E., 2010. Collisional spreading of Enceladus' neutral cloud. Icarus 209, 696–703. doi:10.1016/j.icarus.2010.04.010

Chauvie, S., Guatelli, S., Ivanchenko, V., Longo, F., Mantero, A., Mascialino, B., Nieminen, P., Pandola, L., Parlati, S., Peralta, L., Pia, M.G., Piergentili, M., Rodrigues, P., Saliceti, S., Trindade, A., 2004. Geant4 low energy electromagnetic physics, in: IEEE Symposium Conference Record Nuclear Science 2004. IEEE, pp. 1881–1885. doi:10.1109/NSSMIC.2004.1462612

Cooper, J.F., Johnson, R.E., Mauk, B.H., Garrett, H.B., Gehrels, N., 2001. Energetic ion and electron irradiation of the icy Galilean satellites. Icarus 149, 133–159. doi:10.1006/icar.2000.6498

Desorgher, L., Flückiger, E.O., Gurtner, M., Moser, M.R., Bütikofer, R., 2005. Atmocosmics: A Geant 4 Code For Computing The Interaction Of Cosmic Rays With The Earth's Atmosphere. Int. J. Mod. Phys. A 20, 6802–6804. doi:10.1142/S0217751X05030132

Dougherty, M.K., Achilleos, N., Andre, N., Arridge, C.S., Balogh, A., Bertucci, C., Burton, M.E., Cowley, S.W.H., Erdos, G., Giampieri, G., Glassmeier, K.H., Khurana, K.K., Leisner, J., Neubauer, F.M., Russell, C.T., Smith, E.J., Southwood, D.J., Tsurutani, B.T., 2005. Cassini magnetometer observations during Saturn orbit insertion. Science (80-.). 307, 1266–1270. doi:10.1126/science.1106098

Ferrari, C., Lucas, A., 2016. Low thermal inertias of icy planetary surfaces. Astron. Astrophys. 588, A133. doi:10.1051/0004-6361/201527625

Filacchione, G., Capaccioni, F., McCord, T.B., Coradini, A., Cerroni, P., Bellucci, G., Tosi, F., D'Aversa, E., Formisano, V., Brown, R.H., Baines, K.H., Bibring, J.P., Buratti, B.J., Clark, R.N., Combes, M., Cruikshank, D.P., Drossart, P., Jaumann, R., Langevin, Y., Matson, D.L., Mennella, V., Nelson, R.M., Nicholson, P.D., Sicardy, B., Sotin, C., Hansen, G., Hibbitts, K., Showalter, M., Newman, S., 2007. Saturn's icy satellites investigated by Cassini-VIMS. Icarus 186, 259–290. doi:10.1016/j.icarus.2006.08.001

Filacchione, G., D'Aversa, E., Capaccioni, F., Clark, R.N., Cruikshank, D.P., Ciarniello, M., Cerroni, P., Bellucci, G., Brown, R.H., Buratti, B.J., Nicholson, P.D., Jaumann, R., McCord, T.B., Sotin, C., Stephan, K., Dalle Ore, C.M., 2016. Saturn's icy satellites investigated by Cassini - VIMS. IV. Daytime temperature maps. Icarus. doi:10.1016/j.icarus.2016.02.019

Hamilton, D.P., Burns, J.A., 1994. Origin of Saturn's E Ring: Self-Sustained, Naturally. Science (80-.). 264, 550–553. doi:10.1126/science.264.5158.550

Hand, K.P., Carlson, R.W., 2012. Laboratory spectroscopic analyses of electron irradiated alkanes and alkenes in solar system ices. J. Geophys. Res. Planets 117, n/a-n/a. doi:10.1029/2011JE003888

Hand, K.P., Carlson, R.W., 2011. H2O2 production by high-energy electrons on icy satellites as a function of surface temperature and electron flux. Icarus 215, 226–233. doi:10.1016/j.icarus.2011.06.031

Hendrix, A.R., Cassidy, T.A., Buratti, B.J., Paranicas, C., Hansen, C.J., Teolis, B., Roussos, E., Todd Bradley, E., Kollmann, P., Johnson, R.E., 2012. Mimas' far-UV albedo: Spatial variations. Icarus 220, 922–931. doi:10.1016/j.icarus.2012.06.012

Horanyi, M., Burns, J. a., Hamilton, D.P., 1992. The dynamics of Saturn's E ring particles. Icarus 97, 248–259. doi:10.1016/0019-1035(92)90131-P

Horányi, M., Juhász, A., Morfill, G.E., 2008. Large-scale structure of Saturn's E-ring. Geophys. Res. Lett. 35, 1–5. doi:10.1029/2007GL032726

Howett, C.J.A., Spencer, J.R., Hurford, T., Verbiscer, A., Segura, M., 2012a. PacMan returns: An electron-generated thermal anomaly on Tethys. Icarus 221, 1084–1088. doi:10.1016/j.icarus.2012.10.013

Howett, C.J.A., Spencer, J.R., Hurford, T., Verbiscer, A., Segura, M., 2012b. PacMan returns: An electron-generated thermal anomaly on Tethys. Icarus 221, 1084–1088. doi:10.1016/j.icarus.2012.10.013

Howett, C.J.A., Spencer, J.R., Schenk, P., Johnson, R.E., Paranicas, C., Hurford, T.A., Verbiscer, A., Segura, M., 2011. A high-amplitude thermal inertia anomaly of probable magnetospheric origin on Saturn's moon Mimas. Icarus 216, 221–226. doi:10.1016/j.icarus.2011.09.007

Jessberger, E.K., Stephan, T., Rost, D., Arndt, P., Maetz, M., Stadermann, F.J., Brownlee, D.E., Bradley, J.P., Kurat, G., 2001. Properties of Interplanetary Dust: Information from Collected Samples, in: Interplanetary Dust. Springer Berlin Heidelberg, Berlin, Heidelberg, pp. 253–294. doi:10.1007/978-3-642-56428-4_6

Johnson, R.E., Carlson, R.W., Cooper, J.F., Paranicas, C., Moore, M.H., Wong, M.C., 2004. Radiation effects on the surfaces of the Galilean satellites, in: Bagenal, F., Dowling, T.E., Mckinnon, W.B. (Eds.), Jupiter: The Planet, Satellites and Magnetosphere. Cambridge University Press, Cambridge, pp. 483–508.

Juhász, A., Horanyi, M., 2015. Dust Delivery from Enceladus to the Moons of Saturn, in: AGU Fall Meeting 2015. San Francisco.

Jurac, S., Richardson, J.D., 2007. Neutral cloud interaction with Saturn's main rings. Geophys. Res. Lett. 34, 13–16. doi:10.1029/2007GL029567

Kempf, S., Beckmann, U., Moragas-Klostermeyer, G., Postberg, F., Srama, R., Economou, T., Schmidt, J., Spahn, F., Grün, E., 2008. The E ring in the vicinity of Enceladus I: Spatial distribution and properties of the ring particles. Icarus 193, 420–437. doi:10.1016/j.icarus.2007.06.027

Kempf, S., Beckmann, U., Schmidt, J., 2010. How the Enceladus dust plume feeds Saturn's E ring. Icarus 206, 446–457. doi:10.1016/j.icarus.2009.09.016

Kollmann, P., Roussos, E., Paranicas, C., Krupp, N., Haggerty, D.K., 2013. Processes forming and sustaining Saturn's proton radiation belts. Icarus 222, 323–341. doi:10.1016/j.icarus.2012.10.033

Krimigis, S.M., Mitchell, D.G., Hamilton, D.C., Livi, S., Dandouras, J., Jaskulek, S., Armstrong, T.P., Boldt, J.D., Cheng, A.F., Gloeckler, G., Hayes, J.R., Hsieh, K.C., Ip, W.-H., Keath, E.P., Kirsch, E., Krupp, N., Lanzerotti, L.J., Lundgren, R., Mauk, B.H., McEntire, R.W., Roelof, E.C., Schlemm, C.E., Tossman, B.E., Wilken, B., Williams, D.J., 2004. Magnetosphere Imaging Instrument (MIMI) on the Cassini Mission to Saturn/Titan. Space Sci. Rev. 114, 233–329. doi:10.1007/s11214-004-1410-8

Krivov, A. V., Sremčević, M., Spahn, F., Dikarev, V. V., Kholshevnikov, K. V., 2003. Impact-generated dust clouds around planetary satellites: asymmetry effects. Planet. Space Sci. 51, 251–269. doi:10.1016/S0032-0633(03)00050-3

Livi, R., Goldstein, J., Burch, J.L., Crary, F., Rymer, A.M., Mitchell, D.G., Persoon, A.M., 2014. Multi-instrument analysis of plasma parameters in Saturn's equatorial, inner magnetosphere using corrections for spacecraft potential and penetrating. J. Geophys. Res. Sp. Phys. 119, 3683–3707. doi:10.1002/2013JA019616

Mauk, B.H., Saur, J., Mitchell, D.G., Roelof, E.C., Brandt, P.C., Armstrong, T.P., Hamilton, D.C., Krimigis, S.M., Krupp, N., Livi, S.A., Manweiler, J.W., Paranicas, C.P., 2005. Energetic particle injections in Saturn's magnetosphere. Geophys. Res. Lett. 32, n/a-n/a. doi:10.1029/2005GL022485

Paranicas, C., Carlson, R.W., Johnson, R.E., 2001. Electron bombardment of Europa. Geophys. Res. Lett. 28, 673–676. doi:10.1029/2000GL012320

Paranicas, C., Cooper, J.F., Garrett, H.B., Johnson, R.E., Sturner, S.J., 2009. Europa's Radiation Environment and Its Effects on the Surface, in: Pappalardo, R.T., Mckinnon, W.B., Khurana, K.K. (Eds.), Europa. The University of Arizona Press, Tucson, AZ, pp. 529–544.

Paranicas, C., Roussos, E., Decker, R.B., Johnson, R.E., Hendrix, A.R., Schenk, P., Cassidy, T.A., Dalton, J.B., Howett, C.J.A., Kollmann, P., Patterson, W., Hand, K.P., Nordheim, T.A., Krupp, N., Mitchell, D.G., 2014. The lens feature on the inner saturnian satellites. Icarus 234, 155–161. doi:10.1016/j.icarus.2014.02.026

Paranicas, C., Roussos, E., Krupp, N., Kollmann, P., Hendrix, A.R., Cassidy, T., Johnson, R.E., Schenk, P., Jones, G., Carbary, J., Mitchell, D.G., Dialynas, K., 2012. Energetic charged particle weathering of Saturn's inner satellites. Planet. Space Sci. 61, 60–65. doi:10.1016/j.pss.2011.02.012

Patterson, G.W., Paranicas, C., Prockter, L.M., 2012. Characterizing electron bombardment of Europa's surface by location and depth. Icarus 220, 286–290. doi:10.1016/j.icarus.2012.04.024

Poppe, A.R., 2016. An improved model for interplanetary dust fluxes in the outer Solar System. Icarus 264, 369–386. doi:10.1016/j.icarus.2015.10.001

Porter, S.B., Desch, S.J., Cook, J.C., 2010. Micrometeorite impact annealing of ice in the outer Solar System. Icarus 208, 492–498. doi:10.1016/j.icarus.2010.01.031

Postberg, F., Kempf, S., Hillier, J.K., Srama, R., Green, S.F., McBride, N., Grün, E., 2008. The E-ring in the vicinity of Enceladus II: Signatures of Enceladus in the elemental composition of E-ring particles. Icarus 193, 438–454. doi:10.1016/j.icarus.2007.09.001

Roussos, E., Jones, G.H., Krupp, N., Paranicas, C., Mitchell, D.G., Lagg, A., Woch, J., Motschmann, U., Krimigis, S.M., Dougherty, M.K., 2007. Electron microdiffusion in the Saturnian radiation belts: Cassini MIMI/LEMMS observations of energetic electron absorption by the icy moons. J. Geophys. Res. Sp. Phys. 112, n/a-n/a. doi:10.1029/2006JA012027

Roussos, E., Krupp, N., Krüger, H., Jones, G.H., 2010. Surface charging of Saturn's plasma-absorbing moons. J. Geophys. Res. 115, A08225. doi:10.1029/2010JA015525

Saur, J., Strobel, D.F., 2005. Atmospheres and Plasma Interactions at Saturn's Largest Inner Icy Satellites. Astrophys. J. 620, L115–L118. doi:10.1086/428665

Schaible, M.J., Johnson, R.E., Zhigilei, L.V., Piqueux, S., 2016. High energy electron sintering of icy regoliths: Formation of the PacMan thermal anomalies on the icy Saturnian moons. Icarus 0, 1–13. doi:10.1016/j.icarus.2016.08.033

Schenk, P., Hamilton, D.P., Johnson, R.E., Mckinnon, W.B., Paranicas, C., Schmidt, J., Showalter, M.R., 2011. Plasma , plumes and rings : Saturn system dynamics as recorded in global color patterns on its midsize icy satellites. Icarus 211, 740–757. doi:10.1016/j.icarus.2010.08.016

Selesnick, R.S., 1993. Micro- and macro- signatures of energetic charged particles in planetary magnetospheres. Adv. Sp. Res. 13, 221–230. doi:10.1016/0273-1177(93)90073-K

Smith, B.A., Soderblom, L., Beebe, R., Boyce, J., Briggs, G., Bunker, A., Collins, S.A., Hansen, C.J., Johnson, T. V, Mitchell, J.L., Terrile, R.J., Carr, M., Cook, A.F., Cuzzi, J., Pollack, J.B., Danielson, G.E., Ingersoll, A., Davies, M.E., Hunt, G.E., Masursky, H., Shoemaker, E., Morrison, D., Owen, T., Sagan, C., Veverka, J., Strom, R., Suomi, V.E., 1981. Encounter with saturn: voyager 1 imaging science results. Science (80-.). 212, 163–91. doi:10.1126/science.212.4491.163

Spahn, F., Albers, N., Hörning, M., Kempf, S., Krivov, A. V, Makuch, M., Schmidt, J., Seiß, M., Miodrag Sremčević, 2006. E ring dust sources: Implications from Cassini's dust measurements. Planet. Space Sci. 54, 1024–1032. doi:10.1016/j.pss.2006.05.022

Thomsen, M.F., Van Allen, J.A., 1980. Motion of trapped electrons and protons in Saturn's inner

magnetosphere. J. Geophys. Res. 85, 5831. doi:10.1029/JA085iA11p05831
Young, D.T., Berthelier, J.-J., Blanc, M., Burch, J.L., Bolton, S., Coates, A.J., Crary, F.J., Goldstein, R., Grande, M., Hill, T.W., Johnson, R.E., Baragiola, R.A., Kelha, V., McComas, D.J., Mursula, K., Sittler, E.C., Svenes, K.R., Szegö, K., Tanskanen, P., Thomsen, M.F., Bakshi, S., Barraclough, B.L., Bebesi, Z., Delapp, D., Dunlop, M.W., Gosling, J.T., Furman, J.D., Gilbert, L.K., Glenn, D., Holmlund, C., Illiano, J.-M., Lewis, G.R., Linder, D.R., Maurice, S., McAndrews, H.J., Narheim, B.T., Pallier, E., Reisenfeld, D., Rymer, a M., Smith, H.T., Tokar, R.L., Vilppola, J., Zinsmeyer, C., 2005. Composition and dynamics of plasma in Saturn's magnetosphere. Science 307, 1262–6. doi:10.1126/science.1106151